Int. J. Electrochem. Sci., 17 **(2022)** Article Number: 22126, doi: 10.20964/2022.12.10

International Journal of
ELECTROCHEMICAL
SCIENCE
www.electrochemsci.org

Initial Corrosion Behavior of EH36 Marine Steel in Simulated Polar Marine Environment

Chenghuan Li[1,2], Can Peng[1,2], Xiaohan Li[1,2], Yuwei Liu[2,3], Yang Liu[2], Zhenyao Wang[2,3], Junjun Pai[4], Chuan Wang[2,3,]*

[1] School of Materials Science and Engineering, University of Science and Technology of China(USTC), 110016 Shenyang, China
[2] Institute of Metal Research, Chinese Academy of Sciences(CAS), 110016 Shenyang, China
[3] Liaoning Shenyang Soil and Atmosphere Corrosion of Material National Observation and Research Station, 110016 Shenyang, China
[4] Shandong Key Laboratory of Advanced Aluminium Materials and Technology, 256600 Binzhou, Shandong Province, China
[*]E-mail: cwang@imr.ac.cn

Received: 11 August 2022 / *Accepted:* 23 September 2022 / *Published:* 17 November 2022

The corrosion behavior of grade EH36 steel in a simulated polar marine atmospheric environment (3.5%NaCl) for 10 d was studied using corrosion weight loss, surface morphology analysis, composition analysis, and electrochemical testing techniques. The results demonstrate that the corrosion rate of EH36 steel at low temperatures was high and it was still in the accelerated corrosion stage. After 240 h of corrosion, the corrosion rate was 0.47 $g \cdot m^{-2} \cdot h^{-1}$. The corrosion products were mainly composed of β-FeOOH, Fe_3O_4, and small amounts of γ-FeOOH and α-FeOOH. The corrosion pit depth increased from 8.81 μm in 48 h of corrosion to 31.70 μm in 240 h. The study of the early corrosion behavior and mechanism of EH36 ship plate steel in polar marine atmospheric environment can provide an important reference for the composition design of ship plate steel and its application in marine environments.

Keywords: Atmospheric corrosion; EH36 steel; Electrochemical impedance spectroscopy; Polar environment

1. INTRODUCTION

Owing to increasing international shipping costs, it is becoming extremely difficult to ignore the existence of a global alternative shipping route. If the Arctic shipping routes are opened, a large economic circle around the Arctic, including East Asia and Russia, will be formed, causing significant changes to the international political landscape. The development of the Arctic channel can significantly shorten the voyage from Northeast Asia to North America and Northern Europe and is also more

conducive to the exploration of oil, gas, and mineral resources in the polar environment. [1] The average temperature in January in the Arctic Circle is less than 0 °C, varying between -5 and -35 °C. In contrast, the average temperatures in summer in the Arctic Ocean (July) is close to 10 °C. [2] Climate records show that the highest temperature in the Arctic Ny-Ålesund region from 2006 to 2014 was 13.4 °C, which was recorded in August; whereas the lowest value was -31.5 °C, which was recorded in February. The annual relative humidity (RH) ranges from 60 to 90%. [3] Cyclone activity is weak, making it suitable for maritime shipping and regional businesses. Therefore, one of the greatest challenges developing appropriate material solutions for low-temperature Arctic applications to achieve long-term durability of ship structures.

There is a growing body of research that recognizes the corrosion problem of marine materials in low-temperature environments. Several researchers have focused on marine atmospheric corrosion of metallic materials in the Arctic and subarctic regions. [4-9] For instance, the corrosive characteristics of welded low-carbon steel under simulated Arctic low-temperature conditions were examined by Choi et al. [10-11] and, the results revealed that the severe influence of corrosion on PM in welded joints. In addition, despite the decrease in the seawater temperature, the corrosion rate was not significantly reduced. Chernov studied the short-term corrosion rate of carbon steel in a seawater environment of 0.22 mm/a at 0 ℃. [12] Brauns and Schwenk reported 3.5-years of observations of corrosion in a 9 °C seawater (average) environment near Heligoland, Germany, at a corrosion rate of 0.42 mm/y. [13] Due to its particularity in the Arctic region, some institutions have already conducted out on-site corrosion coupons. [14-15] Therefore, for the safe design of polar marine structures, it is necessary to investigate installation and operation environments and formulate appropriate corrosion management plans.

Grade EH36 low-temperature and high-toughness ship plate steel is mainly used in the manufacture of large offshore platforms, decks of large- and medium-sized ocean-going ships, and other key parts of the hull. Therefore, more attention has been paid to the low-temperature brittleness and fatigue of marine steel; however, [16-18] several scholars are still interested in the corrosion resistance of marine steel. The steel structure of ships sailing in polar regions is be continuously impacted by ice, eroded by wind and waves, and the temperature difference between day and night. Mardare and Benea compared the effects of different polymer coatings on the corrosion resistance of EH36 steel surfaces in the Black Sea marine environment. [19] Vukelic et al. investigated changes in the mechanical properties and surface conditions of AH36 steel butt-welded specimens exposed to a natural marine environment for prolonged periods of time and observed that, pit depths increased significantly during the first 6 months of exposure and sea waves generally had the most severe impact on corrosion. [20] The application environment of ship steel is extremely harsh. The hull shell and offshore platform structural materials running on the ocean not only have to withstand the chemical, electrochemical, and microbial corrosions of seawater but also withstand the impact of large winds and waves and the influence of day and night temperature changes. Several researchers have used laboratory-accelerated tests to study the steel corrosion process. Among the different indoor simulated accelerated methods, the dry–wet alternate accelerated test is the most efficient method. During the day and night cycles, the temperature and humidity vary regularly, which changes the thickness of the water film on the steel surface and affects the electrochemical process between the metal surface and the surrounding environment.

In this study, 3.5% NaCl solution was used as the simulated polar seawater, with 20 and -40 ℃ as the extreme temperature values of the accelerated dry-wet cycle test. The corrosion behavior of EH36 steel in a low-temperature marine atmosphere was studied using scanning electron microscopy (SEM), and white light interference (MicroXAM) was used to observe the morphology of the corrosion products and the surface morphology of EH36 steel after the removal of corrosion products. We hope to further understand the corrosion process of steel in this low-temperature marine atmosphere and to provide theoretical guidance for the safe service of materials through this study.

2. EXPERIMENTAL

2.1 Sample preparation

The experiments were conducted using low-temperature carbon steel (EH36, Table 1), which is the most commonly used ship navigation system in cold areas. Before the test, the samples were cut into blocks of 50 mm × 25 mm × 6 mm for the corrosion weight loss test, and the surfaces of the specimens were progressively ground with silicon carbide (SiC) papers up to 1200 grit, degreased with acetone, rinsed with deionized water and alcohol, dried in cool air, and placed in a desiccator for 24 h. Finally, a precision electronic balance (accuracy 0.1 mg) was used to measure the weight of the sample.

Table 1. Chemical compositions of EH36 steel (*wt*.%)

C	Al	Si	P	S	Ti	Cr	Mn	Ni	Cu	Nb
0.16	0.027	0.31	0.013	0.002	0.012	0.078	1.47	0.016	0.021	0.028

The remaining samples were cut into 10 mm× 10 mm× 6 mm blocks for the electrochemical tests (three parallel samples), with a wire attached to the back, immersed in epoxy resin, and sealed. Each sample was ground to 1200 mesh using a grinding machine and thereafter cleaned and dried according to the aforementioned steps.

2.2 Wet–dry cyclic accelerated test

The remote and desolate Arctic has a harsh climate, and the wet–dry cyclic test was performed in a climate test chamber to simulate the corrosive conditions faced by the offshore platform and ship structures in the polar marine climate. The model of the experimental equipment was LRHS-225C-LJS. To simulate the effects of alternating day and night ultraviolet (UV) exposure in polar regions, we added a 15 W quartz UV lamp and a blackboard to the cavity (Figure 1 (a)). The plate divided the chamber into

two layers, one dark and one light, with slits on the sides to allow airflow to circulate. The UV irradiation intensity of the upper exposed sample surface was 61 μW/cm^2, as measured using a UVAB photometer (TM213). The intensity value was obtained from the highest average UV-B radiation intensity in the air of the Arctic Spitsbergen islands in the summer (1998-2000). [21]

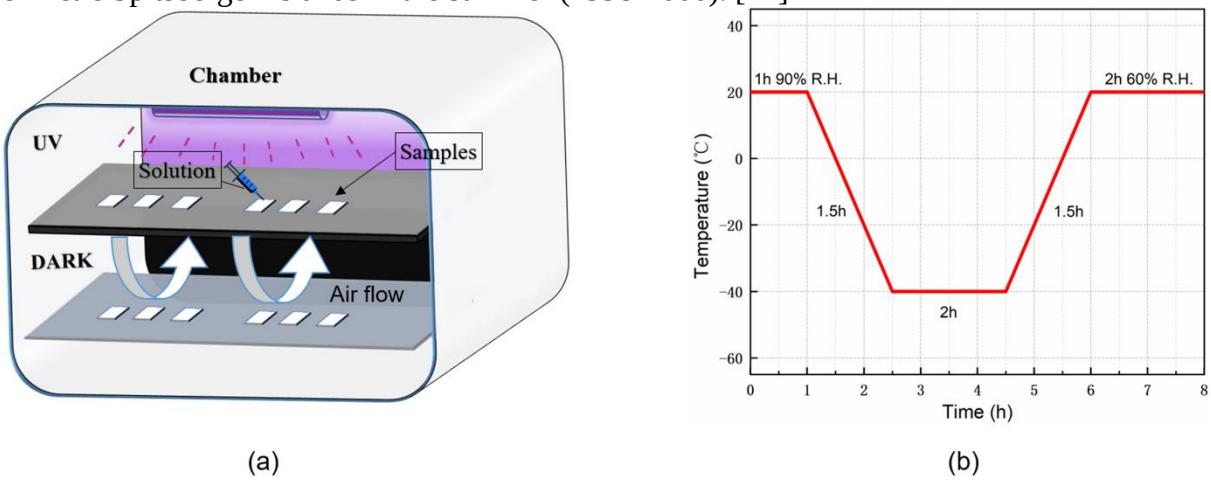

Figure 1. (a) Schematic diagram of wet-dry cyclic accelerated test equipment, (b) Temperature and humidity time of one test cycle (8 h): (1) wet, 1 h (20 ℃, 90% RH); (2) cooling, 1.5 h; (3) low temperature, 2 h (-40 ℃); (4) warming up, 1.5 h; and (5) dry, 2 h (20 ℃, 60% RH).

The test cycle conditions were set as shown in Figure 1 (b). The program settings were as follows: (1) wet, 1 h (20 ℃, 90% RH); (2) cooling, 1.5 h; (3) low temperature, 2 h (-40 ℃); (4) warming up, 1.5 h; and (5) dry, 2 h (20 ℃, 60% RH). Eight hours made one cycle, and 30 cycles were performed during the test period. We set 90% RH at the beginning of the cycle, such that the water film on the sample surface would condense into ice when entering the low-temperature cycle. In addition, to simulate the continuous deposition of seawater on the sample surface, a pipette gun was used to deposit 20 μL/cm^2 of 3.5% NaCl solution on the surface of the samples every three cycles. After every depositing, the samples were dried in an oven at 35 ℃ for 20 min. After performing the corrosion test for 48, 96, 144, 192, and 240 h, the samples were removed from the test chamber.

2.3 Weight loss

The weight loss was determined by weighing the difference in the weight of the samples before and after corrosion. According to GB/T 16545-2015, the scraped samples were put in the pickling solution, which contained 500mL hydrochloric acid + 3.5 g hexadimethyltetramine + 500 mL distilled water, and thereafter brushed and cleaned for 10 min. They were subsequently washed with distilled water and alcohol, blow dried with warm air, and stored in a desiccator at least 24 h before weighing.

2.4 Surface morphology and composition analysis

A portable camera was used to capture the macroscopic surface topographies of the corroded samples. The morphologies of the corrosion products were observed through SEM. The elemental content and distribution of the rust layer were analyzed using an energy dispersive spectrometer (Inspect F). The phase composition of the corrosion products was analyzed through X-ray diffraction (XRD), and the XRD with a Cu Kα target was performed in the range of 10–80°, at 50 kV, 250 mA, and a scanning speed of 10°/min. After removing the corrosion products, the surface topography was analyzed using white light interference (MicroXAM).

2.5 Electrochemical measurements

Electrochemical testing was performed using an electrochemical workstation with a traditional three-electrode system in 3.5% NaCl. The reference electrode was a saturated calomel electrode, the auxiliary electrode was a Pt piece, and the working electrode was the sample to be tested (1 cm^2). Before EIS measurements, the samples were immersed in the salted solution for 30 min to ensure that the testing process reached a steady state. Thereafter, EIS measurements were conducted at frequencies ranging from 10^5 to 10^{-2} Hz, and the amplitude of the AC voltage was 10 mV.

3. RESULTS AND DISCUSSION

3.1 Weight loss

The weight loss of corrosion represented by the weight loss per unit area before and after corrosion. The calculation formula of corrosion weight loss as follows:

$$w = \frac{w_0 - w_t}{s} \quad (1)$$

where w is the weight loss (g/m^2), w_0 is the initial mass (g), w_t is the rust removed mass (g), S is the surface area of the test specimen (m^2).

The corrosion rate of the sample changes with time, which can be obtained by the following formula:

$$V_d = \frac{W_n - W_{n-1}}{t_n - t_{n-1}} \quad (2)$$

where V_d represents the average corrosion rate ($g \cdot m^{-2} \cdot h^{-1}$), W_n is the weight loss (g), t is the corrosion time (h), and n is the period of samples.

The corrosion dynamics of carbon steel can be described by equation:

$$W = At^n \quad (3)$$

where W denotes the weight loss (g/m^2), t is the corrosion time, and A and n are correlation coefficients. When n is greater than 1, corrosion is accelerated and the corrosion products are unprotective.

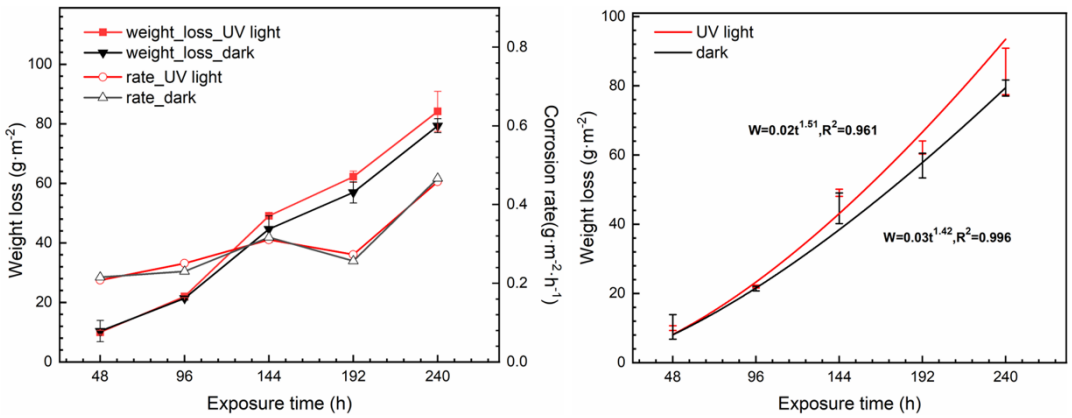

Figure 2. (a) Variation of weight loss and corrosion rate of EH36 steel in dark and UV irradiation after 48, 96, 144, 192, 240h exposure in simulated polar marine atmosphere, (b) Variation of corrosion weight loss fitting of EH36 steel in dark and UV irradiation after 48, 96, 144, 192, 240h exposure in simulated polar marine atmosphere.

Figure 2 (a) shows the change in the corrosion weight loss and corrosion rate of the samples with and without UV irradiation. The fitting results for the corrosion weight loss are shown in Figure 2 (b). As shown in Figure 2 (a), the weight loss curve with or without UV irradiation begins to diverge from 96 h, indicating that the influence of UV irradiation on corrosion weight loss requires time. With the help of macroscopic images, it was observed that the effect of UV on weight loss was reflected only after the rust layer covered the entire sample. In both cases, the value of n was greater than 1, indicating that corrosion was accelerated. Other scholars have reported the impact of UV light; however, in the tested environment, we did not observe any differences. [22-23] This may be attributed to the particularity of our environment, or the differences will appear over a long period of time.

3.2. Surface morphology and cross-sectional analysis

Figure 3 shows the evolution of the surface rust layer with and without UV light. It can be observed that the rust layer on the sample surface increases with the increase in the number of cycles, the surface color changes from orange to orange, and thereafter gradually turns orange yellow. After 96 h of corrosion, the rust layer completely covered the sample surface. When the corrosion time was extended to 96 h, the sample was exposed to a brown inner rust layer, and the rust layer on the surface of the sample gathered into a sheet and was uneven. At the beginning of the test, pitting rust appeared on the rust layer on the surface of the sample. With the passage of time, the rust on the bottom layer gradually covered the surface, and the new rust formed pits. This phenomenon lasted for 144 h. In addition, it can be observed from Figure 3 that there was no obvious difference in macro morphology whether there is UV light or not.

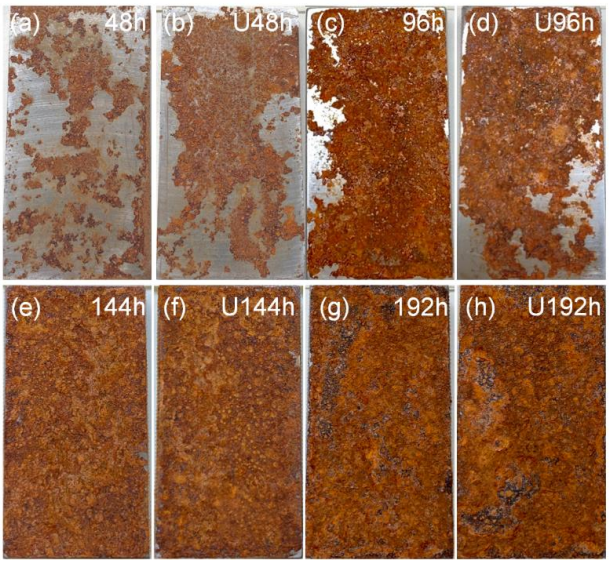

Figure 3. Macroscopic morphology evolution of the rust layer of EH36 steel with and without UV irradiation after 48, 96, 144, 192h cycles exposure in simulated polar marine atmosphere: dark for 48 h (a), 96 h (c), 144h (e), 192h (g), and UV irradiation for 48 h (b), 96 h (d), 144h (f), 192h (h).

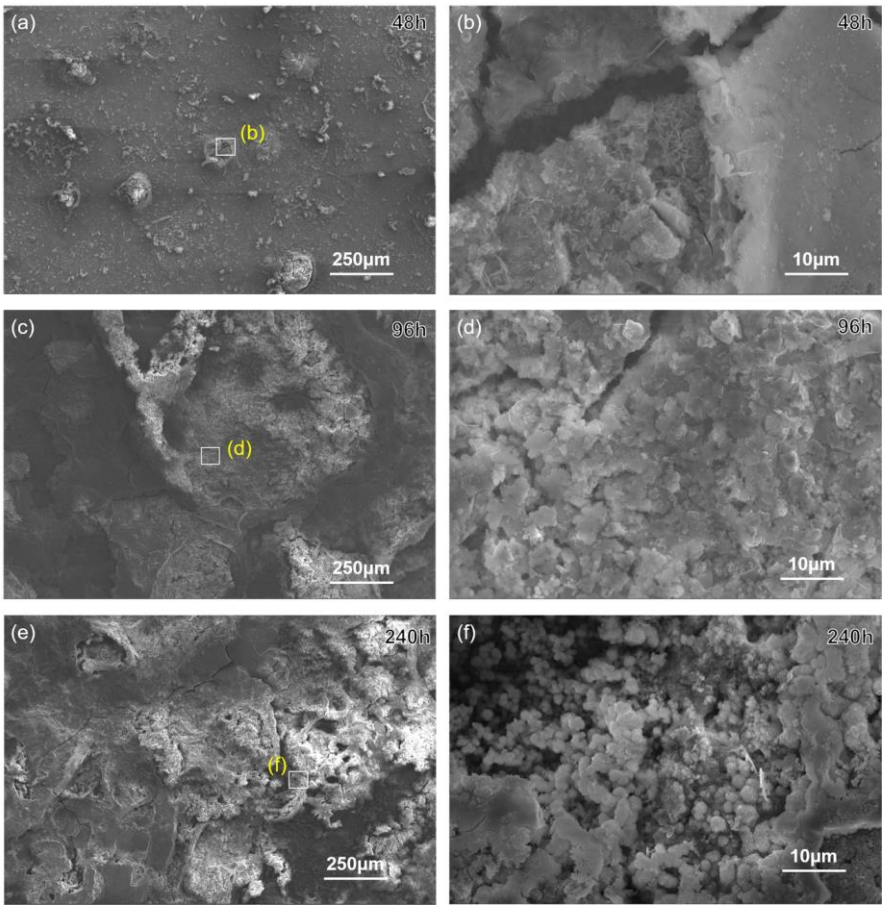

Figure 4. Micro-morphology of rust layer of EH36 steel after 48, 96, 240h cycles exposure with dark in simulated polar marine atmosphere. 48 h (**a**), (**b**), 96 h (**c**), (**d**), 240 h (**e**), (**f**).

Figure 4 shows the SEM images of the EH36 specimen after a low-temperature dry-wet etching cycle. As shown in Figure 4 (a), the corrosion products on the surface of the early samples exhibit clear point-like protrusions; with an increase in the periodic cycle, the number of protrusions gradually increases and forms a complete rust layer. Figure 4 (b) shows that the structure of the pit-like protrusion was annular, and several cracks radiated from the center to the surroundings. Therefore, a few needle-like structures were observed in the protrusions. This indicates that the product was β-FeOOH, [24-25] which is prone to forming voids that promote corrosion. After 96 h of corrosion, the SEM images of the corrosion products demonstrated that the needle-like products began to transform into lumps, and cotton ball-like products were formed on the surface of the EH36 rust layer. Previous studies have also reported that α-FeOOH is cotton-ball-like. [26]

From the overall trend, in the early stage of corrosion, the corrosion product clusters were small, the structure was loose, and there was a certain distance between them. Corrosive media, such as chlorine, tend to accumulate in these locations and penetrate the substrate. Further corrosion plays a role in promoting corrosion. As the number of cycles increased, the corrosion products grew and aggregated into lumps. In comparison to needle-like β-FeOOH, α-FeOOH has a cluster-like crystal form, and the crystals are small and dense, which has a certain protective effect.

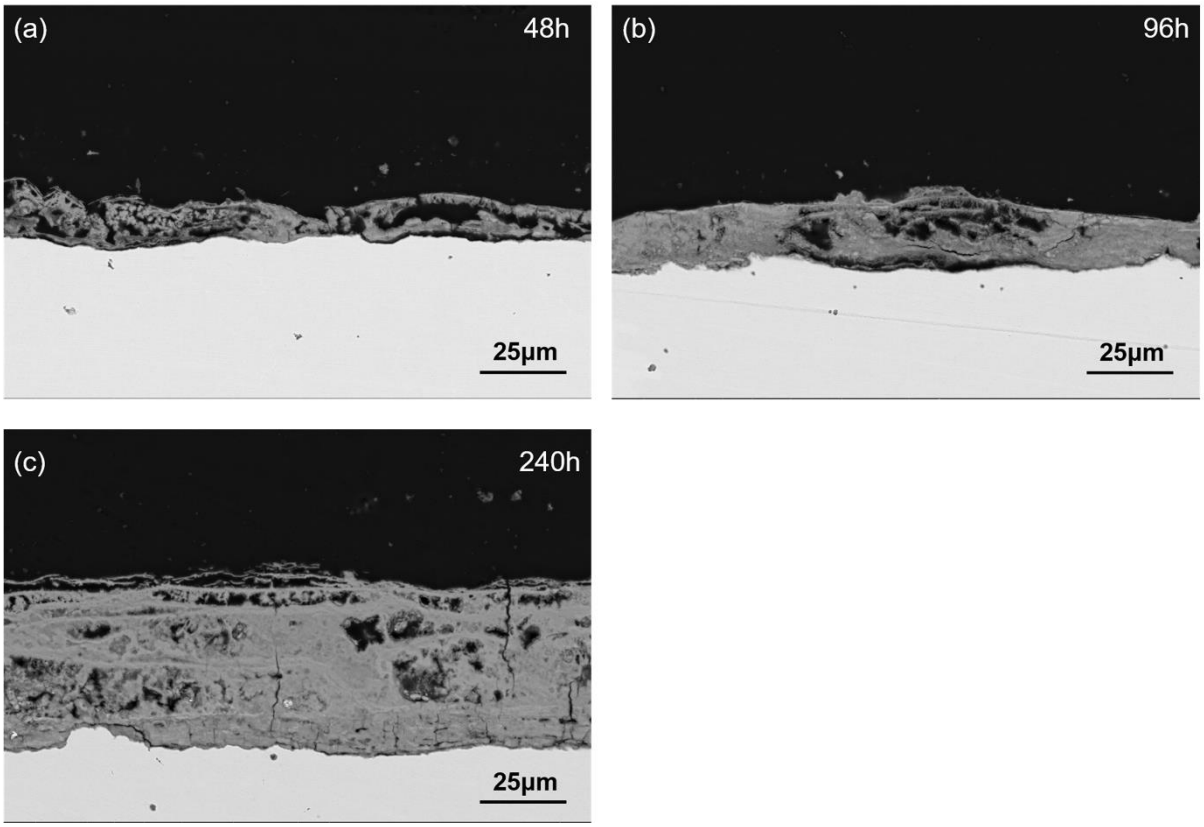

Figure 5. Cross-sectional morphology of the rust layer of EH36 steel after 48, 96, 240h cycles exposure with dark in simulated polar marine atmosphere. (a) 48 h, (b) 96 h, (c) 240 h.

The cross-sectional morphological analysis is shown in Figure 5. With the extension of time, the thickness of the rust layer after 240 h of corrosion was more than three times that after 48 h, indicating

that EH36 has a fast corrosion rate under simulated low-temperature marine atmospheric conditions. The initial corrosion products exhibited weak adhesion with the substrate. In addition, the unstable outer rust layer easily fell off, resulting in the thinning of the thickness. The rust layer became dense after 96 h of corrosion, which is consistent with the macro-morphology results, as shown in Figure 5 (b). In addition, cracks can be observed in the corrosion products, which are not conducive to protection. Furthermore, some cracks extended down to the matrix and acted as transport channels for Cl^-, resulting in further corrosion.

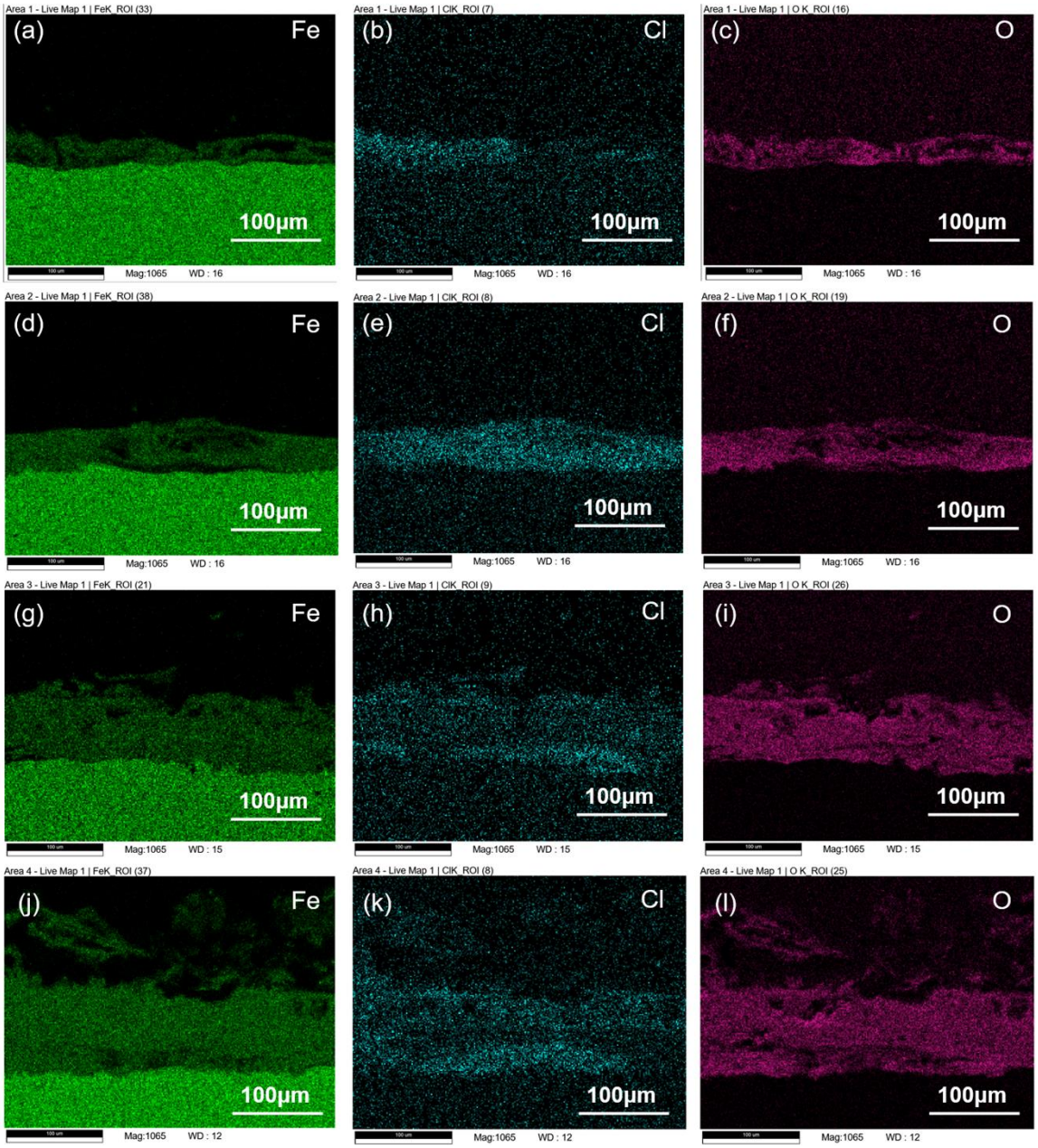

Figure 6. Elemental distribution of iron, chlorine and oxygen in the cross section of the rust layer of EH36 steel after 48, 96, 144, 240h cycles exposure with dark in simulated polar marine atmosphere. 48 h (**a**), (**b**)**,** (**c**), 96 h (**d**), (**e**), (**f**), 144 h (**g**), (**h**), (**i**), 240 h (**j**), (**k**), (**l**).

Figure 6 shows the elemental distributions of Fe, Cl, and O in the rust layer cross-section. The distribution of these key elements can help us to understand the development of the corrosion process. The distribution of Fe made it easy to observe the structure of the corrosion products of EH36 because they are basically iron oxides. [27-28] In contrast, the distributions of Cl and O were different, which gave us an understanding of the occurrence of the corrosion process. As shown in Figures 6 (a) and (c), the initial Cl distribution was uniform and filled the entire corrosion product layer. As the thickness of the corrosion product layer increased, the number of cracks gradually increased, and the distribution of Cl gradually became characteristic, distributed at the bottom of the rust layer (where it meets the substrate), and at the junction between the surface of the rust layer and the outer layer (Figures 6 (h) and (k)). It can also be observed from Figures 6 (j) and (k) that Cl was enriched in the pores of the corrosion products, which may be due to the longitudinal cracks near the pores that act as Cl channels. Thus, Cl can penetrate deep into the matrix layer, thereby accelerating corrosion. Table 2 indicates that the Cl content does not change significantly at the initial stage with time. After 240 h of corrosion, the proportion of chlorine in the rust layer increased significantly compared to that in the initial stage.

Table 2. Elemental content at the same multiple`s area in Fig. 6. (*wt.%*)

	Time cycle			
Element	48h	96h	144h	240h
O	7.18	8.32	14.45	15.95
Cl	0.52	0.48	1.02	1.51
Fe	92.30	31.20	84.43	82.54

Figures 7 and 8 show the surface topography of the samples after removal of the corrosion products. It can be observed that there were some pits formed on the surface of the sample, and its evolution law also corresponds to the evolution law of the surface rust layer: at the initial stage, the pits continue to grow, and at the later stage, the pits gather into blocks and the growth of the pit depth decreases. Local pits gradually gathered and formed uniform corrosion. Figure 8 shows that with an increase in corrosion time, the pit depth gradually deepened. The depth was 8.81 μm in the 24th hour, and thereafter increased rapidly to 21.5 μm in the next 24 h, and subsequently increased to 31.70 μm in the next 240 h. At the beginning, the pit depth changed significantly, which may be due to the fact that the rust layer formed was not sufficiently thick and Cl^- could penetrate directly into the matrix. Therefore, pitting corrosion could occur. After 96 h of exposure, owing to the formation of complete and uniform corrosion products on the surface, the penetration of Cl^- was hindered and the growth of the pit depth decreased.

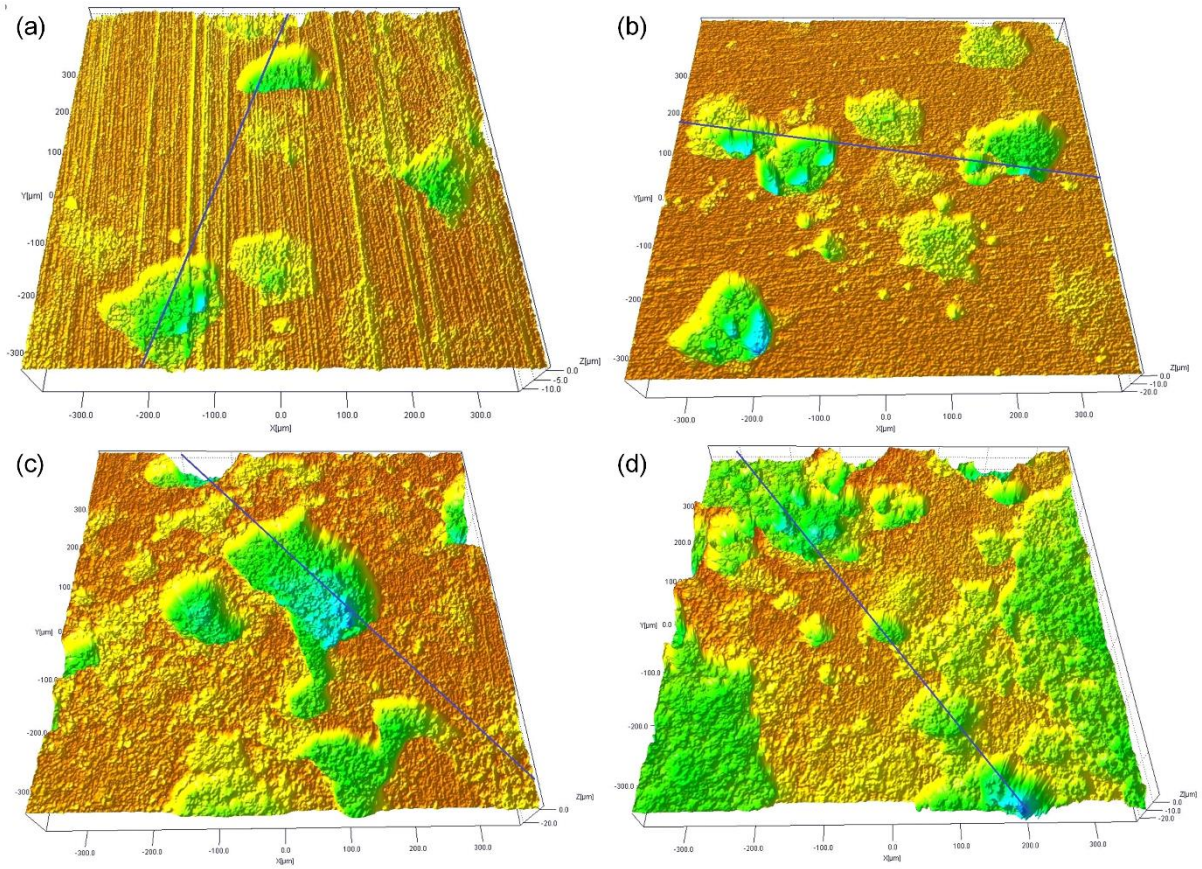

Figure 7. Morphological evolution of pitting pits after corrosion product removal after 48, 96, 144, 240h cycles exposure with dark in simulated polar marine atmosphere. (a) 48 h, (b) 96 h, (c) 144 h, (d) 240 h.

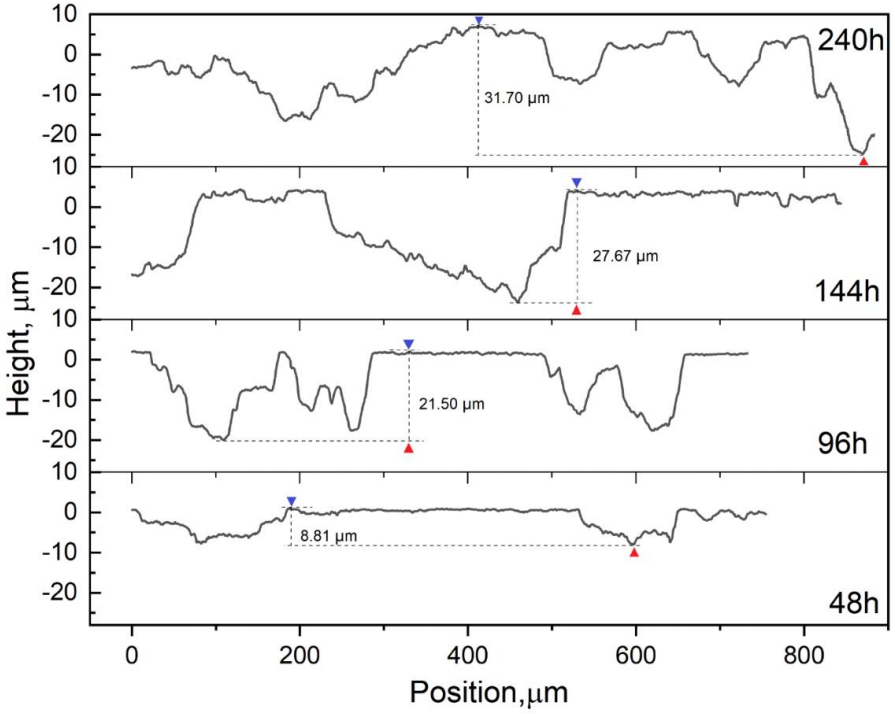

Figure 8. Pit depth of horizontal line in Fig. 7.

3.3 Composition of the rust layer

To obtain the evolution process of the corrosion products and clarify the mechanism of the corrosion process, the obtained XRD pattern is shown in Figure 9. After 48 h of corrosion, the main corrosion products were β-FeOOH and Fe_3O_4. The composition of the corrosion products changed slightly with time. After 240 h of corrosion, the γ-FeOOH and α-FeOOH diffraction peaks were detected in the corrosion product. In the NaCl solution environment, the corrosion products were mainly oxides and oxyhydroxides of iron. Therefore, it was demonstrated that β-FeOOH can provide a channel for corrosive media, such as Cl^-, making it easy to penetrate the corrosion product layer and directly contact the substrate, destroy the formed dense rust layer, and accelerate the corrosion of the substrate. γ-FeOOH and α-FeOOH are two relatively stable iron oxyhydroxides, which can enhance the corrosion resistance of the rust layer.

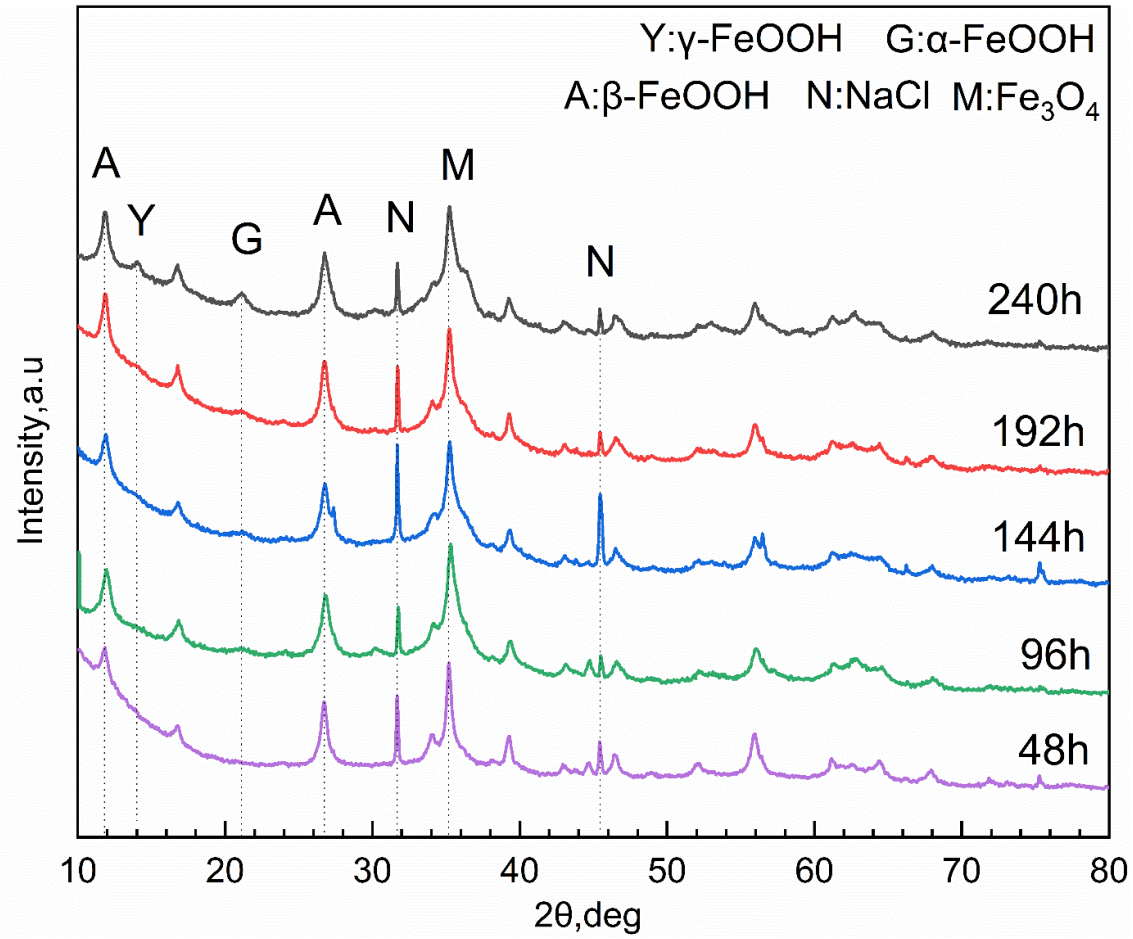

Figure 9. XRD pattern of powdered rust formed on EH36 steel formation after 48, 96, 144, 192h, 240h cycles exposure with dark in simulated polar marine atmosphere.

In this study, the corrosion rate increased with the corrosion time. After 240 h, γ-FeOOH and α-FeOOH were detected in the corrosion products; however, the corrosion rate did not decrease, which may be due to their lower content, and the main corrosion products were still β-FeOOH.

3.4 EIS measurement

EIS is often used to study the reaction ability of the metal/film interface and the changing characteristics of the rust layer. [29] The Nyquist and Bode diagrams of the EH36 carbon steel after different corrosion times are shown in Figure 10. In the Nyquist diagram (Figure 10 (a)), the diameter of the impedance loop gradually decreased, indicating that the protection of corrosion products gradually decreased. The Bode impedance diagram (Figure 10 (b)) shows that at the lowest frequency, |Z| decreases with the corrosion time. In the phase-angle diagram (Figure 10 (b)), only one maximum peak was observed in the low-frequency range. This indicates that the corrosion resistance of steel is gradually reduced owing to the lack of a protective film on the steel surface.

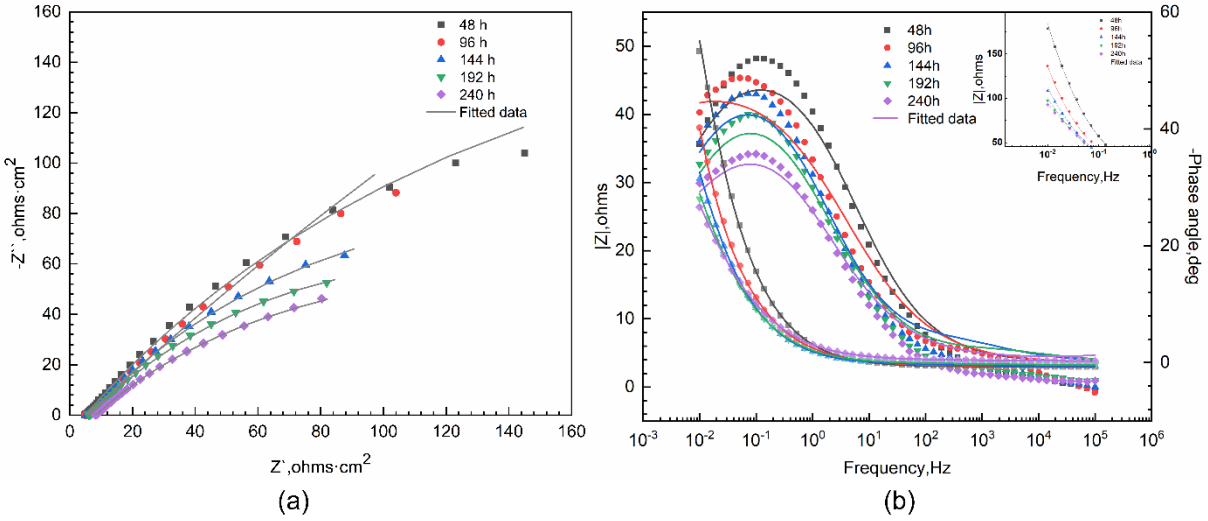

Figure 10. Impedance spectrum of the rusted EH36 steel after different exposed time with dark in simulated polar marine atmosphere: (a) Nyquist plots, (b) Bode impedance and phase angle plots. The solid lines represent the fitted results.

The two equivalent electric circuit models shown in Figure 11 were used to fit the EIS curves. The term R_s represents the solution resistance, R_r is the resistance of insoluble corrosion products, R_{ct} is the charge transfer resistance, and Q_r and Q_{dl} are the capacitance of the corrosion products and the double-layer capacitance of the electrolyte solution and steel substrate surface, respectively. The fitted parameters are listed in Table 2. After 48 h of exposure, the rust layer did not completely cover the surface, and bare metal was in direct contact with the solution. With the passage of time, a complete rust layer was formed on the metal surface, and the value of R_{ct} continued to decrease, indicating that the corrosion rate gradually increased, which is consistent with the above results. The value of R_r reached a maximum at 240 h and 5.63 $\Omega \cdot cm^2$, which is significantly higher than the value previously obtained. This may be attributed to the relatively stable corrosion products at 240 h.

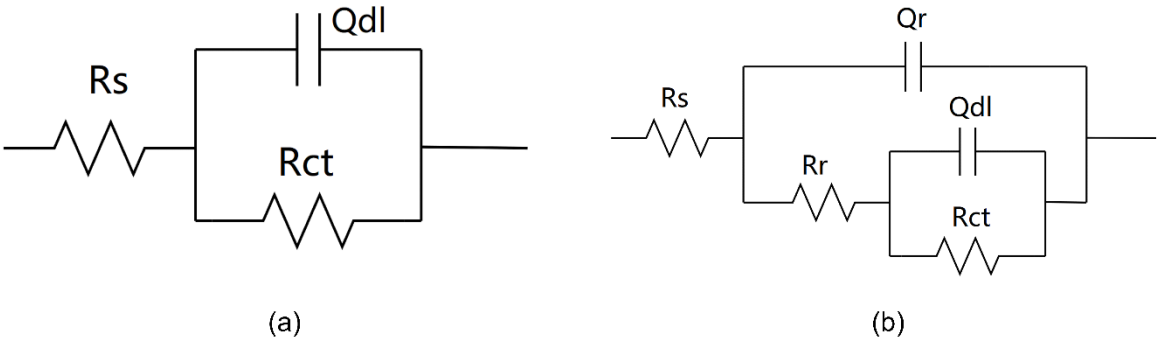

Figure 11. Two equivalent circuits for fitting impedance data: (a) fitting data with only one capacitive loop, (b) fitting data with two capacitive loops.

Table 3. EIS[a] test fitting parameters of EH36 steel after 48, 96, 144, 192h, 240h cycles exposure with dark in simulated polar marine atmosphere.

	Time cycle				
Parameter	48h	96h	144h	192h	240
$R_s(\Omega \cdot cm^2)$	4.89	4.92	5.27	5.86	6.81
$Q_r(F \cdot cm^{-2})$		3.07×10^{-3}	1.04×10^{-2}	5.92×10^{-3}	2.59×10^{-2}
n_r		0.65	0.56	0.57	0.55
$R_r(\Omega \cdot cm^2)$		1.72	1.72	0.98	5.63
$Q_{dl}(F \cdot cm^{-2})$	2.33×10^{-2}	2.99×10^{-2}	2.75×10^{-2}	3.22×10^{-2}	1.31×10^{-2}
n_{dl}	0.80	0.60	0.62	0.59	0.62
$R_{ct}(\Omega \cdot cm^2)$	541.8	526.2	307.4	242.5	241.3
$\sum\chi^2(\times 10^{-4})$	8.97	3.48	0.75	0.72	0.43

[a] EIS, electrochemical impedance spectroscopy

3.5 Corrosion Mechanism Analysis

It is well known that the corrosion tendency increases with an increase in temperature. However, some studies have reported that the existence of a liquid film caused by the freezing and thawing process of ice and snow in the Antarctic low-temperature environment accelerates corrosion. [30] In this study, the polar marine climate environment was simulated through high- and low-temperature dry-wet cycles. The Cl^- content is an important factor that affects corrosion. In the liquid membrane system, the solution contains a certain amount of oxygen, and oxygen reduction is the main cathode reaction, whereas the anode is dominated by the dissolution of iron:

$$Fe - 2e^- \rightarrow Fe^{2+} \quad (4)$$

$$O_2 + H_2O + 4e^- \rightarrow 4OH^- \quad (5)$$

$$Fe(OH)_2 + Cl^- \rightarrow Fe(ClO) + H_2O + e^- \quad (6)$$

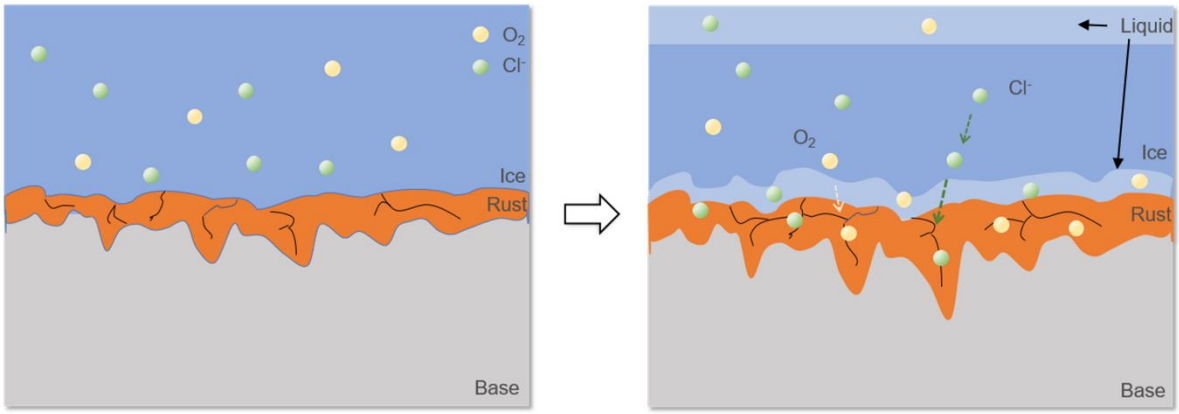

Figure 12. Corrosion mechanism of substrate under icing: (a) freezing, (b) melting

Owing to the slow reaction at low temperatures, the sample was too late to form a protective corrosion product. The Cl-content in the thin liquid film gradually increased, accelerating the reaction of Equation (4). The reaction of the two products of $FeCl_2$, which thereafter hydrolyzes to produce $FeOH_2$, finally produces β-FeOOH. The environmental characteristics of low temperature and high chlorine also explain the large number of rust layer components, β-FeOOH. As shown in Figure 12 (b), during the heating stage, ice melts preferentially at the junction with the matrix, and Cl^- can diffuse, resulting in the uniform corrosion of the surface of the matrix. In addition, the existence of longitudinal cracks in the rust layer enables Cl^- and oxygen to extend longitudinally through the cracks, thus enriching at the bottom and accelerating corrosion. These observations were consistent with the sectional characteristics. It has been reported by scholars that freezing treatment will cause cracks in the steel material in the early stage of the corrosion process, and then expand on the surface. [31-32]

Despite its limitations, this study adds to our understanding of the corrosion processes under the ice interface. We demonstrated that there is still considerable corrosion under the ice layer. The freezing of the liquid film makes it easier for chloride ions to accumulate at the interface, which increases the corrosion rate before the emergence of protective rust products, resulting in the uniform corrosion of EH36 steel.

4. CONCLUSIONS

In this study, the corrosion behavior of EH36 steel in simulated low-temperature marine atmospheric environment with high-low temperature dry wet cycle for 240h is studied. The main conclusions are as follows:

1. The corrosion rate of EH36 steel in a simulated low-temperature marine atmospheric environment is not low and it continues to increase with time. The corrosion rate was 0.47 $g \cdot m^{-2} \cdot h^{-1}$ after 240 h of corrosion.

2. The main corrosion products generated in this environment were β-FeOOH and Fe_3O_4. A small amount of γ-FeOOH began to appear after 240 h of corrosion, and the amount of protective α-

FeOOH was also very small. The early corrosion products were loose, porous, and unprotective, and the corrosion process was still in the accelerated stage after 240 h.

3. Cl^- tends to be distributed on the surface and near the substrate in the rust layer with enrichment, and the corrosion form is from pitting corrosion to uniform corrosion. This may be due to the fact that during the melting of the ice layer, the ice layer at the matrix first melted into a liquid film, resulting in the enrichment of chloride ions.

ACKNOWLEDGEMENTS
The investigation is supported by the Bintech-IMR R&D Program (No. GYY-JSBU-2022-006) and Liaoning Shenyang Soil and Atmosphere Corrosion of Material National Observation and Research Station.

References

1. E. Bekkers, J. F. Francois and H. Rojas-Romagosa, *The Econ. J.*, 128 (2018) 1095.
2. V. C. Khon, I. Mokhov, M. Latif, V. A. Semenov and W. Park, *Clim. Change*, 100 (2010) 757.
3. S. Wang, M. Ding, W. Sun, L. Bian, L. U. Changgui, C. Xiao, T. Wei, D. Zhang, T. Zhang and Y. Wang, *J. Glaciol. Geocryology*, 39 (2017) 479.
4. B. Chernov, I. Chaves, A. Nugmanov and R. Melchers, *Corrosion*, 74 (2018) 1466.
5. G. Biefer, *Mater. Perform.*, 20 (1981) 16.
6. M. Morcillo, B. Chico, D. Fuente, E. Almeida, G. Joseph, S. Rivero and B. Rosales, *Cold Reg. Sci. Technol.*, 40 (2004) 165.
7. Y. Ma, L. Ying, and F. Wang, *Corros. Sci.*, 51 (2009) 997.
8. A. Mikhailov, P. Strekalov and Y. M. Panchenko, *Prot. Met.*, 44 (2008) 644.
9. J. Marco, M. Gracia, J. Gancedo, M. Martın-Luengo and G. Joseph, *Corros. Sci.*, 42 (2000) 753.
10. B. Chico, D. D. L. Fuente and M. Morcillo, *Bol. Soc. Esp. Ceram. Vidrio*, 39 (2000) 329.
11. Y. Y. Choi, and M. H. Kim, *RSC Adv.*, 8 (2018) 30155.
12. B. B. Chernov, and S. A. Ponomarenko, *Prot. Met.*, 27 (1991) 612.
13. E. Brauns, and W. Schwenk, *Stahl Eisen*, 87 (1967) 713.
14. Y. Panchenko, A. Marshakov, L. Nikolaeva, T. Igonin and V. Kovtanyuk, *Corros. Eng. Sci. Technol.*, 56 (2021) 703.
15. R. E. Melchers, *Corros. Eng. Sci. Technol.*, 56 (2021) 736.
16. Y. Wang, J. Liu, J. Hu, Y. Garbatov and C. G. Soares, *Int. J. Fatigue*, 142 (2021) 105896.
17. W. Zhao, G. Feng, B. J. Leira and H. Ren, *J. Energy Resour. Technol.*, 144 (2022) 14.
18. Q. Zhu, P. Zhang, X. Peng, L. Yan and G. Li, *Mater.*, 14 (2021) 6621.
19. L. Mardare, and L. Benea, *IOP Conf. Ser.: Mater. Sci. Eng.*, 572 (2019) 012007.
20. G. Vukelic, G. Vizentin, S. Ivosevic and Z. Bozic, *Eng. Failure Anal.*, 135 (2022) 106132.
21. H. Svendsen, A. Beszczynska-Møller, J. O. Hagen, B. Lefauconnier, V. Tverberg, S. Gerland, J. B. Ørbøk, K. Bischof, C. Papucci, M. Zajaczkowski, R. Azzolini, O. Bruland, C. Wiencke, J.-G. Winther and W. Dallmann, *Polar Res.*, 21 (2002) 133.
22. L. Song, Z. Chen, *Corros. Sci.*, 86 (2014) 318.
23. C. B. Breslin, D. D. Macdonald, J. Sikora and E. Sikora, *Electrochim. Acta*, 42 (1997) 127.
24. N. T. Goldman, C. B. Koch and A. Singer, *Clays Clay Miner.*, 50 (2002) 186.
25. S. Nasrazadani, *Corros. Sci.*, 39 (1997) 1845.
26. J. Castaño, C. Botero, A. Restrepo, E. Agudelo, E. Correa and F. Echeverría, *Corros. Sci.*, 52 (2010) 216.

27. Y. Xu, Q. Zhou, L. Liu, Q. Zhang, S. Song and Y. Huang, *Corros. Eng., Sci. Technol.*, 55 (2020) 579.
28. L. Ziyun, W. Gui, L. Siwei, D. Peichang, H. Jiezhen, D. Junhao and X. Jingming, *J. Chin. Soc. Corros. Prot.*, 40 (2020) 463.
29. F. Corvo, J. Minotas, J. Delgado and C. Arroyave, *Corros. Sci.*, 47 (2005) 883.
30. Z. Cui, F. Ge, X. Wang and *J. Chin. Soc. Corros. Prot.*, 42 (2022) 403.
31. Y. Shen, *Int. J. Electrochem. Sci.*, 13 (2018) 6310.
32. H. Li, *Int. J. Electrochem. Sci.*, 12 (2017) 11077.